Inorganic Chemistry

Article

Cite This: Inorg. Chem. 2019, 58, 9706−9712

pubs.acs.org/IC

1-D Chain Tungstotellurate Hybrids Constructed from Organic-Ligand-Connecting Iron−Lanthanide Heterometal Encapsulated Tetrameric Polyoxotungstate Units

Jian-Cai Liu,[†] Jun-Wei Zhao,*[,‡] and Yu-Fei Song*[,†]

[†]State Key Laboratory of Chemical Resource Engineering, Beijing Advanced Innovation Center for Soft Matter Science and Engineering, Beijing University of Chemical Technology, Beijing 100029, People's Republic of China

[‡]Henan Key Laboratory of Polyoxometalate Chemistry, College of Chemistry and Chemical Engineering, Henan University, Kaifeng, Henan 475004, People's Republic of China

Supporting Information

ABSTRACT: A family of inorganic−organic hybrid one-dimensional (1-D) chain iron−lanthanide (Ln) heterometal encapsulated tungstotellurates $[H_2N(CH_3)_2]_8K_2Na_4[Ln_2(Ac)_2(H_2O)_4Fe_2(Hpdca)_2(B\text{-}\beta\text{-}TeW_9O_{33})_2]\text{-}[Ln_2(H_2O)_8Fe_2(Hpdca)_2(B\text{-}\beta\text{-}TeW_9O_{33})_2]\cdot 50H_2O$ [Ln = Eu^{3+} (**1**), Tb^{3+} (**2**), Dy^{3+} (**3**), Er^{3+} (**4**), HAc = acetate acid, H_2pdca = 2,5-pyridinedicarboxylic acid] were prepared using a facile "one-pot" reaction. The molecular structures of **1**−**4** consist of an intriguing organic-ligand-connecting Fe−Ln heterometal inserted tetrameric unit $[Ln_2(Ac)_2(H_2O)_4Fe_2(Hpdca)_2(B\text{-}\beta\text{-}TeW_9O_{33})_2][Ln_2(H_2O)_8Fe_2(Hpdca)_2(B\text{-}\beta\text{-}TeW_9O_{33})_2]^{14-}$. Appealingly, the tetrameric unit is composed of two sandwich-type subunits $[Ln_2(Ac)_2(H_2O)_4Fe_2(Hpdca)_2(B\text{-}\beta\text{-}TeW_9O_{33})_2]^{8-}$ and $[Ln_2(H_2O)_8Fe_2(Hpdca)_2(B\text{-}\beta\text{-}TeW_9O_{33})_2]^{6-}$, in which each sandwich-type subunit can be regarded as a derivative of two Ln-organic complexes substituting two external Fe^{III} ions in the classic Krebs-type $[Fe_4(H_2O)_{10}(\beta\text{-}TeW_9O_{33})_2]^{4-}$ fragment. Furthermore, adjacent tetrameric units are interconnected into a 1-D chain arrangement by $Hpdca^-$ bridges. **1**−**4** represent the first examples of Fe−Ln heterometal encapsulated tungstotellurates. Comprehensive magnetic measurements of **3** imply the possible single-molecule magnet properties in **3** with an estimated relaxation time $\tau_0 \approx 6.06 \times 10^{-6}$ s at $H_{dc} = 0$ Oe and $\tau_0 \approx 6.97 \times 10^{-5}$ s at $H_{dc} = 1500$ Oe. In addition, the solid-state photoluminescence spectra of **1** and **2** at room temperature exhibit the typical f−f transitions of Ln cations. The Commission International d'Eclairage (CIE) color coordinates of (0.540 24, 0.442 44) for **1** and (0.428 71, 0.428 30) for **2** along with the correlated color temperatures of 1995 and 3278 K, dominant wavelengths of 586 and 578 nm, and color purities of 95.09% and 57.27% for **1** and **2** are obtained.

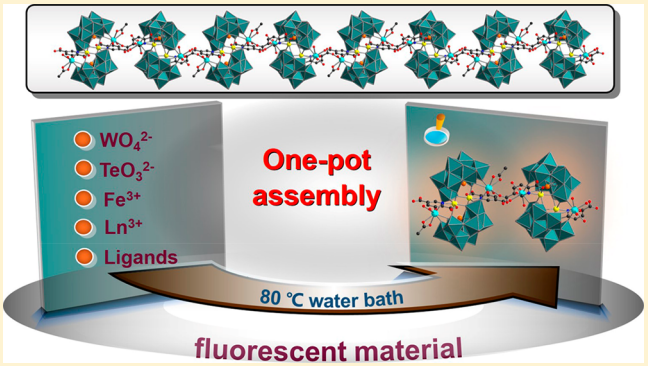

INTRODUCTION

Polyoxometalates (POMs) are a remarkable class of polyanionic metal-oxo clusters condensed by early transition metals (Mo^{VI}, W^{VI}, V^V, Nb^V, or Ta^V) with fascinating architectural characteristics and a wide range of promising applications.[1−4] Since the first example of this class $(NH_4)_3PMo_{12}O_{40}$ was published by Berzelius in 1826,[5] there has been a continuous upsurge of interest in the exploration and fabrication of novel POMs, giving rise to a tremendous number of versatile POM-based functional derivatives.[6−9] Among them, tungstotellurates (TTs) have become an appealing synthetic target in recent years for the unique lone electron pair stereochemical effect of TeO_3^{2-} heteroanion templates. Note that various lacunary TT building blocks are discovered during the course of preparation, which show stronger coordination ability as inorganic ligands to accommodate transition-metal (TM) or lanthanide (Ln) cations. Currently, significant progresses have been successively achieved on TM-encapsulated TTs, ranging from classic tri- and tetra-TM-sandwiched dimeric species to the nanosized multi-TM-inserted aggregates.[10−14] In contrast, the Ln-containing TTs (LnTTs) represent a newly arisen realm, as the first $[\{(TeO_3)W_{10}O_{34}\}_8\{Ce_8(H_2O)_{20}\}(WO_2)_4(W_4O_{12})]^{48-}$ was discovered in 2013,[15] which shows an interesting change from single giant polyoxoanion to inorganic hollow sphere in the dilute water or acetone solution. This seminal work fascinates chemists to prepare more LnTTs from diverse structures to material properties. The past several years have witnessed continuous development in LnTTs. Generally, the advances in this field can be classified into three categories: (i) the purely inorganic aggregates involving the multi-Ce^{3+}-containing octamers $[\{(TeO_3)W_{10}O_{34}\}_8\{Ce_8(H_2O)_{20}\}$-

Received: March 2, 2019
Published: July 18, 2019

DOI: 10.1021/acs.inorgchem.9b00618
Inorg. Chem. 2019, 58, 9706−9712

Table 1. Crystallographic Data and Structural Refinements for 1−4

	1	2	3	4
empirical formula	$C_{48}H_{212}Eu_4Fe_4K_2N_{12}Na_4O_{214}Te_4W_{36}$	$C_{48}H_{212}Tb_4Fe_4K_2N_{12}Na_4O_{214}Te_4W_{36}$	$C_{48}H_{212}Dy_4Fe_4K_2N_{12}Na_4O_{214}Te_4W_{36}$	$C_{48}H_{212}Er_4Fe_4K_2N_{12}Na_4O_{214}Te_4W_{36}$
Fw	12 512.68	12 540.52	12 463.12	12 573.88
crystal system	triclinic	triclinic	triclinic	triclinic
space group	$P\bar{1}$	$P\bar{1}$	$P\bar{1}$	$P\bar{1}$
a, Å	13.3515(4)	13.3385(5)	13.3027(6)	13.2906(5)
b, Å	17.6064(3)	17.6697(4)	17.6233(8)	17.5513(7)
c, Å	26.7352(6)	26.6886(9)	26.6321(8)	26.6288(10)
α, deg	108.431(2)	108.618(2)	108.430(4)	107.997(4)
β, deg	96.535(2)	96.541(3)	96.594(3)	96.863(3)
γ, deg	97.427(2)	97.094(2)	97.479(4)	97.994(3)
V, Å^{-3}	5831.8(3)	5836.2(3)	5791.6(4)	5762.6(4)
Z	1	1	1	1
μ, mm^{-1}	19.621	19.743	19.963	20.224
$F(000)$	5606.0	5614.0	5527.0	5626.0
T, K	293(2)	293(2)	293(2)	293(2)
limiting indices	$-15 \le h \le 14$	$-15 \le h \le 15$	$-15 \le h \le 15$	$-15 \le h \le 15$
	$-20 \le k \le 20$	$-20 \le k \le 21$	$-19 \le k \le 20$	$-20 \le k \le 19$
	$-31 \le l \le 30$	$-31 \le l \le 31$	$-31 \le l \le 29$	$-31 \le l \le 31$
no. of reflections collected	44 825	43 820	43354	46111
no. of independent reflections	20 473	20 630	20 227	20 198
R_{int}	0.0581	0.0516	0.0418	0.0475
data/restrains/parameters	20 473/60/1225	20 630/80/1233	20 227/20/1230	20 198/24/1238
goodness-of-fit on F^2	0.995	1.049	1.059	1.053
final R indices $[I > 2\sigma(I)]$	$R_1 = 0.0509$	$R_1 = 0.0593$	$R_1 = 0.0447$	$R_1 = 0.0445$
	$wR_2 = 0.1100$	$wR_2 = 0.1476$	$wR_2 = 0.1029$	$wR_2 = 0.0961$
R indices (all data)	$R_1 = 0.0801$	$R_1 = 0.0821$	$R_1 = 0.0564$	$R_1 = 0.0600$
	$wR_2 = 0.1220$	$wR_2 = 0.1652$	$wR_2 = 0.1084$	$wR_2 = 0.1024$

$(WO_2)_4(W_4O_{12})]^{48-}$ and $[Ce_{10}Te_8W_{88}O_{298}(OH)_{12}(H_2O)_{40}]^{18-}$, as well as the first Dawson-type tetramer $[H_{16}\{Ln(H_2O)_5(TeW_{18}O_{64})\}_4]^{28-}$ (Ln = Eu^{3+}, Gd^{3+});[15−17] (ii) the rare inorganic−organic carboxyl-decorated hybrids $[Ln_2(H_2O)_4(pica)_2W_2O_5][(Ln(H_2O)W_2(Hpica)_2O_4)(B\text{-}\beta\text{-}TeW_8O_{30}H_2)_2]_2^{4-}$ (Ln = La^{3+}, Ce^{3+}, Nd^{3+}, Sm^{3+}, Eu^{3+});[18] (iii) the pioneering organometal-Ln heterometallic functional species $\{[Sn(CH_3)W_2O_4(IN)][(B\text{-}\alpha\text{-}TeW_8O_{31})Ln(H_2O)(Ac)]_2\}_2^{20-}$ (Ln = Ce^{3+}, Pr^{3+}, Nd^{3+}, Sm^{3+}, Eu^{3+}, Gd^{3+}, Tb^{3+}) and $[Ln_2(OH)(B\text{-}\alpha\text{-}TeW_7O_{28})Sn_2(CH_3)_4(W_5O_{18})]_2^{14-}$ (Ln = Er^{3+}, Yb^{3+}, Ho^{3+}, Y^{3+}).[19,20] It's noteworthy that all these findings were synthesized from the one-pot assembly of simple commercial materials, which highlights the potential of effective combination of Ln linkers and TeO_3^{2-} heteroanion templates to create novel LnTTs. However, no study has been conducted in the area of TM−Ln heterometallic TTs. As is known, researchers are continuously in pursuit of introducing functional TM and Ln cations into one system to fabricate novel heterometallic materials with both of their outstanding features such as catalysis, magnetism, optics, and so on.[21−23] Nevertheless, the development in the TM−Ln heterometallic TTs is relatively slow, which is probably caused by the synthetic obstacles that the strongly oxyphilic preference of Ln cations toward nucleophilic TTs may preclude the formation of TM−Ln species. Besides, the reaction of TM ions with POM precursors is liable to produce classic sandwich-type TTs. Thus, it is still a challenging task in creating neoteric TM−Ln heterometallic TT materials.

To cope with these challenges, recently, we began to explore the TM−Ln−TT system in aqueous solution to prepare novel organic−inorganic hybrid TM−Ln heterometallic TT materials with intriguing structures and possible functional synergistic effect between TM and Ln cations in the tunable role of organic components based on the following considerations. First, the one-pot assembly strategy is employed in our reaction system, because it has been proved as an effective synthetic method of constructing TM or Ln-encapsulated TT derivatives; also, this synthetic strategy can provide an enormous unpredictability of creating novel TM−Ln heterometallic TT materials by the multicomponent synergistic effect of in situ-generated TT fragments, TM cations, Ln cations, and organic components. Second, functional acetate acid (HAc) and 2,5-pyridinedicarboxylic acid (H_2pdca) ligands possess flexible O and N coordination sites and have strong coordination ability and versatile coordination modes, which are highly conducive to link TM cations, Ln cations, and in situ-generated TT fragments together to form unseen TM−Ln inserted poly(TT)s by virtue of coordination and connection functionalities of functional organic ligands. Moreover, the incorporation of multicarboxylic H_2pdca ligands can also allow the agglomeration of multimetal centers into inorganic−organic hybrid multinuclear or high-dimensional extended heterometallic TT materials. Third, the auxiliary dimethylamine hydrochloride not only can improve the reaction activities of TM and Ln cations in the TT system but also protonated dimethylamine cations can serve as the large counter cations to stabilize the structures of complicated heterometallic TT materials. Thus, a series of organic-ligand-connecting Fe^{III}−Ln heterometallic TTs $[H_2N(CH_3)_2]_8K_2Na_4[Ln_2(Ac)_2(H_2O)_4Fe_2(Hpdca)_2(B\text{-}\beta\text{-}TeW_9O_{33})_2]\text{-}[Ln_2(H_2O)_8Fe_2(Hpdca)_2(B\text{-}\beta\text{-}TeW_9O_{33})_2]\cdot 50H_2O$ [Ln = Eu^{3+} (**1**), Tb^{3+} (**2**), Dy^{3+} (**3**), Er^{3+} (**4**)] were prepared for the first time under mild acidic condition from the one-pot assembly of

DOI: 10.1021/acs.inorgchem.9b00618
Inorg. Chem. 2019, 58, 9706−9712

$Na_2WO_4{\cdot}2H_2O$, K_2TeO_3, $Eu(NO_3)_3{\cdot}6H_2O$, and $Fe(NO_3)_3{\cdot}9H_2O$ in the presence of organic components of dimethylamine hydrochloride, acetic acid, and H_2pcda. The most striking structural feature of **1**−**4** is that they all comprise an Hpdca-connective Fe−Ln heterometallic tetrameric TT unit $[Ln_2(Ac)_2(H_2O)_4Fe_2(Hpdca)_2(B\text{-}\beta\text{-}TeW_9O_{33})_2]$-$[Ln_2(H_2O)_8Fe_2(Hpdca)_2(B\text{-}\beta\text{-}TeW_9O_{33})_2]^{14-}$, while each tetrameric unit is constructed by two distinct organic-ligand-decorated heterometallic sandwich-type subunits $[Ln_2(Ac)_2(H_2O)_4Fe_2(Hpdca)_2(B\text{-}\beta\text{-}TeW_9O_{33})_2]^{8-}$ and $[Ln_2(H_2O)_8Fe_2(Hpdca)_2(B\text{-}\beta\text{-}TeW_9O_{33})_2]^{6-}$. Moreover, neighboring Hpdca-connective Fe−Ln heterometallic tetrameric TT units in **1**−**4** are interconnected by $Hpdca^-$ ligands into the one-dimensional (1-D) infinite chain motif. Systematic magnetic measurements of **3** indicate the weak single-molecule magnet behavior. Moreover, the photoluminescence spectra and decay behaviors of **1** and **3** were studied at room temperature, which originates from the contribution of f−f transitions of Ln cations, and the chromaticity coordinates, color temperatures, dominant wavelengths as well as color purities for **1** and **2** are also calculated.

RESULTS AND DISCUSSION

Structural Description. **1**−**4** were prepared by the simple one-pot reaction of $Na_2WO_4{\cdot}2H_2O$, K_2TeO_3, and Ln^{3+} and Fe^{3+} ions in the assistance of organic ingredients (dimethylamine hydrochloride, HAc, and H_2pcda) in the pH range of 3.8−4.5. The formation of amorphous precipitations after the reaction system cooled to room temperature (first heating at 80 °C for 90 min) led to the low yield of targeted compounds. After filtration, lamellar crystals were obtained with the evaporation of filtration. The crystals are in good purity, and the phase purity of **1**−**4** is verified by the good accordance of the experimental powder X-ray diffraction (PXRD) patterns with their simulated patterns from single-crystal X-ray diffraction (Figure S1). Crystallographic data and structural refinements for **1**−**4** are listed in Table 1. Bond valence sum (BVS) calculations illustrate that the oxidation states of all W, Fe, and Ln elements in **1**−**4** are +6, +3, and +3, respectively (Table S1). The XPS analyses of **1** and **3** were performed to further confirm the valences of W, Ln, and Fe atoms (Figure 1). The peaks around 37.69 and 35.49 eV for **1** and around 37.87 and 35.77 eV for **3** correspond to the W $4f_{5/2}$ and W $4f_{7/2}$ of the W^{6+} centers.[24] The signals at 725.89 and 711.60 eV for **1** and at 725.06 and 711.50 eV for **3** are ascribed to the Fe $2p_{1/2}$ and Fe $2p_{3/2}$ of the Fe^{3+} cations.[23] Besides, the Eu $3d_{3/2}$ and Eu $3d_{5/2}$ binding energies of 1164.89 and 1135.29 eV for **1** indicate that the Eu centers are +3.[25] As for **3**, two peaks at 157.07 and 153.71 eV are attributed to the Dy^{3+} ($3d_{3/2}$) and Dy^{3+} ($3d_{5/2}$).[26]

1−**4** are isostructural and all crystallize in the triclinic space group $P\bar{1}$, featuring the 1-D chain arrangement constructed from adjacent Hpdca-connective Fe^{III}−Ln heterometallic tetrameric TT units $[Ln_2(Ac)_2(H_2O)_4Fe_2(Hpdca)_2(B\text{-}\beta\text{-}TeW_9O_{33})_2]$-$[Ln_2(H_2O)_8Fe_2(Hpdca)_2\ (B\text{-}\beta\text{-}TeW_9O_{33})_2]^{14-}$ by double Ln−O−C bonds. To our knowledge, **1**−**4** are the first examples of TM−Ln heterometallic TT derivatives. Here, only **4** is described as a representation in detail. The molecular structural unit of **4** consists of an inorganic−organic hybrid Fe−Er heterometallic tetrameric polyanion $[Er_2(Ac)_2(H_2O)_4Fe_2(Hpdca)_2\ (B\text{-}\beta\text{-}TeW_9O_{33})_2][Er_2(H_2O)_8Fe_2(Hpdca)_2(B\text{-}\beta\text{-}TeW_9O_{33})_2]^{14-}$ (**4a**) (Figure 2a), eight $[H_2N(CH_3)_2]^+$ cations, two K^+ cations, four Na^+ cations, and 50 lattice water molecules. **4a** can be viewed as a fusion of two asymmetric heterometallic dimeric

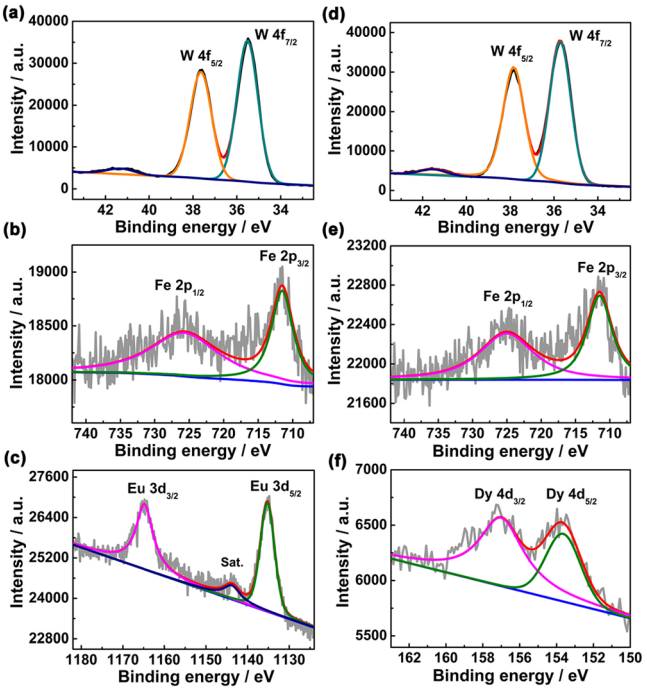

Figure 1. (a) The XPS spectrum for W $4f_{7/2}$ and W $4f_{5/2}$ in **1**. (b) The XPS spectrum for Eu $3d_{5/2}$ and Eu $3d_{3/2}$ in **1**. (c) The XPS spectrum for Fe $2p_{3/2}$ and Fe $2p_{1/2}$ in **1**. (d) The XPS spectrum for W $4f_{7/2}$ and W $4f_{5/2}$ in **3**. (e) The XPS spectrum for Dy $3d_{5/2}$ and Dy $3d_{3/2}$ in **3**. (f) The XPS spectrum for Fe $2p_{3/2}$ and Fe $2p_{1/2}$ in **3**.

subunits $[Er_2(Ac)_2(H_2O)_4Fe_2\ (Hpdca)_2(B\text{-}\beta\text{-}TeW_9O_{33})_2]^{8-}$ and $[Er_2(H_2O)_8Fe_2(Hpdca)_2(B\text{-}\beta\text{-}TeW_9O_{33})_2]^{6-}$ through Er−O−C bonds (Figure 2a−c). Note that both subunits consist of two trivacant $[B\text{-}\beta\text{-}TeW_9O_{33}]^{8-}$ ({TeW_9}) fragments sandwiching two external Er^{3+} and two internal Fe^{3+} centers; however, the selective coordination of organic components to metal centers makes two subunits distinct. Specifically, the central belt of the $[Er_2(Ac)_2(H_2O)_4Fe_2(Hpdca)_2(B\text{-}\beta\text{-}TeW_9O_{33})_2]^{8-}$ subunit is composed of two mono-Ac-chelating $[Er1(Ac)(H_2O)_2]^{2+}$ cations and two mono-Hpdca-chelating $[Fe1(Hpdca)]^{2+}$ cations (Figure S2), whereas the central belt of the $[Er_2(H_2O)_8Fe_2(Hpdca)_2(B\text{-}\beta\text{-}TeW_9O_{33})_2]^{6-}$ subunit contains two $[Er(H_2O)_4]^{3+}$ cations and two mono-Hpdca-chelating $[Fe(Hpdca)]^{2+}$ cations (Figure S3). The preferential binding of the Ac^- ligand to one Er^{3+} ion leads to the different coordination environments, though two crystallographically independent Er^{3+} ions display the octa-coordinate severely distorted bicapped trigonal prism configurations. The $Er1^{3+}$ ion is surrounded by three O atoms (O15, O35, and O6A) located at the vacant sites of two {TeW_9} fragments, three carboxyl O atoms [two from Ac^- ligands (O4, O72) and one from the bridging $Hpdca^-$ ligand (O64)], and two water ligands (O1W, O2W) [Er1−O: 2.262(9)−2.430(11) Å], while the $Er2^{3+}$ ion coordinates with three terminal O atoms (O48B, O13B, and O21) from two {TeW_9} segments, one carboxyl O atom of a $Hpdca^-$ ligand (O34), and four water molecules (O3W−O6W) [Er2−O: 2.261(9)−2.423(9) Å]. Two crystallographically independent Fe^{3+} ions adopt the hexafold distorted octahedral geometry via combining with four terminal O atoms from two {TeW_9} fragments, one carboxyl O atom, and one N atom from the $Hpdca^-$ connector. The Fe1−O (N) and Fe2−O (N) bond lengths fall into the ranges of 1.932(7)−2.130(9) and 1.931(8)−2.104(10) Å, respectively.

DOI: 10.1021/acs.inorgchem.9b00618
Inorg. Chem. 2019, 58, 9706−9712

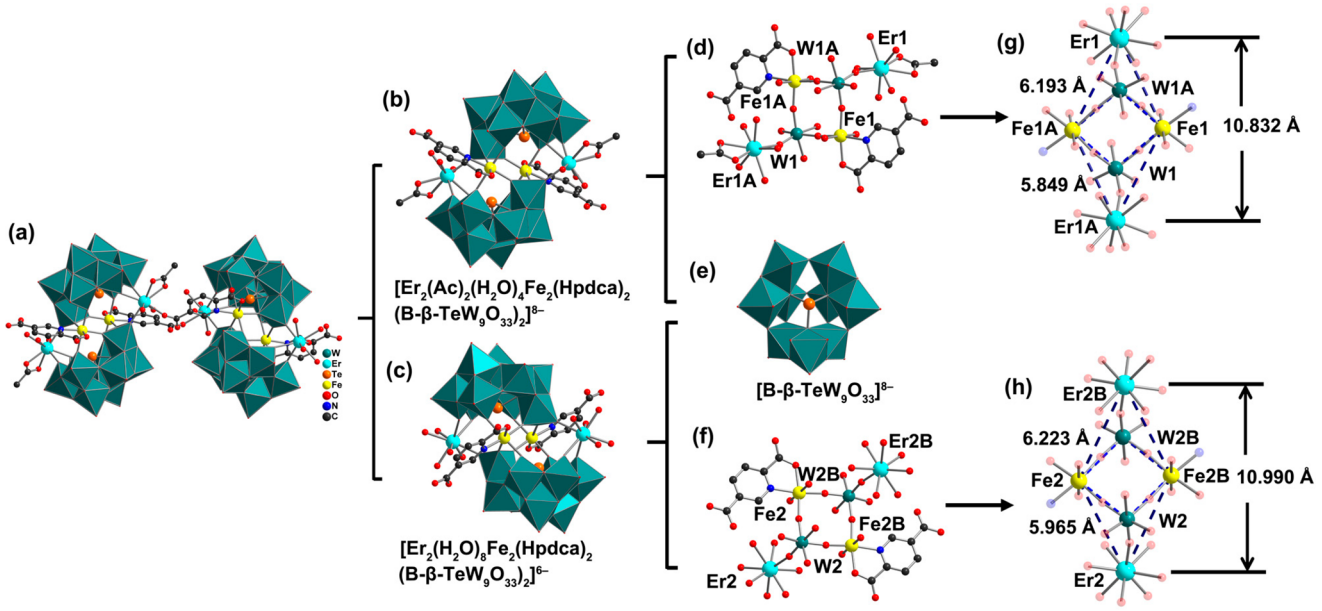

Figure 2. (a) The molecular structure unit of **4a**. (b) The asymmetrical subunit $[Er_2(Ac)_2(H_2O)_4Fe_2(Hpdca)_2(B\text{-}\beta\text{-}TeW_9O_{33})_2]^{8-}$. (c) The asymmetrical subunit $[Er_2(H_2O)_8Fe_2(Hpdca)_2(B\text{-}\beta\text{-}TeW_9O_{33})_2]^{6-}$. (d) The connection of two $[Er1(Ac)(H_2O)_2]^{2+}$ cations and two $[Fe1(Hpdca)]^{2+}$ cations by two W atoms. (e) The trivacant $[B\text{-}\beta\text{-}TeW_9O_{33}]^{8-}$ fragment. (f) The connection of two $[Er2(H_2O)_4]^{3+}$ cations and two $[Fe2(Hpdca)]^{2+}$ cations by two W atoms. (g) The double parallelogram-like heterometallic centers with edge lengths of 5.894 and 6.193 Å of $\{Fe_2Er_2\}$ group and 3.742 and 3.731 Å of $\{Fe_2W_2\}$ group in the asymmetrical subunit $[Er_2(Ac)_2(H_2O)_4Fe_2(Hpdca)_2(B\text{-}\beta\text{-}TeW_9O_{33})_2]^{8-}$. (h) The double parallelogram-like heterometallic centers with edge lengths of 5.965 and 6.223 Å of $\{Fe_2Er_2\}$ group and 3.738 and 3.737 Å of $\{Fe_2W_2\}$ group in the asymmetrical subunit $[Er_2(H_2O)_8Fe_2(Hpdca)_2(B\text{-}\beta\text{-}TeW_9O_{33})_2]^{6-}$. The atoms with the suffix A and B are generated by the symmetry operations where A: $-x, -y, -z$ and B: $1-x, -y, 1-z$.

To our knowledge, the typical tetra-TM substituted sandwich-type species $[TM_4(H_2O)_{10}(\beta\text{-}XW_9O_{33})]^{n-}$ (X = As^{III}, Sb^{III}, Se^{IV}, Te^{IV}; TM = Fe^{III}, Mn^{II}, Co^{II}, Ni^{II}, Cu^{II}, Zn^{II}, Cd^{II}) and their derivatives have been extensively studied.[22,27,28] In **1**−**4**, not only the coordination water molecules on two internal Fe^{3+} ions are completely substituted by $Hpdca^-$ ligands but also two external Fe^{3+} ions are replaced by Er−organic segments, which give rise to the TM−Ln heterometallic sandwich-type Krebs-type structure. More interestingly, the heterometallic centers are decorated by various organic components. Such coordination phenomenon is unusual in the field of POM-based TM−Ln heterometallic derivatives. Additionally, the Er^{3+} and Fe^{3+} ions in the sandwich belt capture other two W atoms derived from two $\{TeW_9\}$ moieties to generate a double-parallelogram-like 3d−4f−5d heterometallic cluster (Figure 2d−f). In this cluster, each W atom connects one Er^{3+} and two Fe^{3+} ions via three μ_2-O atoms, leading to the tetranuclear parallelogram-like clusters $\{Fe_2Er_2\}$ and $\{Fe_2W_2\}$ (Figure 2g−h). For $\{Fe_2Er_2\}$ groups, two Er^{3+} and two Fe^{3+} ions are distributed in an alternating mode and situated at the corners of the parallelogram with two edge lengths of 5.894 and 6.193 Å in the subunit $[Er_2(Ac)_2(H_2O)_4Fe_2(Hpdca)_2(B\text{-}\beta\text{-}TeW_9O_{33})_2]^{8-}$, as well as two edge lengths of 5.965 and 6.223 Å in the subunit $[Er_2(H_2O)_8Fe_2(Hpdca)_2(B\text{-}\beta\text{-}TeW_9O_{33})_2]^{6-}$ (Figures S4 and S5), respectively. Similarly, the edge lengths of $\{Fe_2W_2\}$ parallelograms are individually 3.742 and 3.731 Å, and 3.738 and 3.737 Å (Figures S4 and S5). The coordination mode between the metal centers in the sandwich belt is reminiscent of the Fe^{III}−Ln tungstoantimonates $[Ln(H_2O)_8]_2[Fe_4(H_2O)_8(thr)_2][B\text{-}\beta\text{-}SbW_9O_{33})_2]\cdot 22H_2O$ [Ln = Pr^{3+}, Nd^{3+}, Sm^{3+}, Eu^{3+}, Gd^{3+}, Dy^{3+}, Lu^{3+}, thr = threonine],[22] which contains a rhomb-like $\{Fe^{III}_4\}$ group chelated by two thr ligands. Nevertheless, the $\{Fe_2Er_2\}$ heterometallic clusters functionalized by Ac^- and $Hpdca^-$ ligands in **4a** make them special in contrast with the previously reported $\{Fe^{III}_4\}$ group.

The neighboring polyanionic units $[Er_2(Ac)_2(H_2O)_4Fe_2(Hpdca)_2(B\text{-}\beta\text{-}TeW_9O_{33})_2]$-$[Er_2(H_2O)_8Fe_2(Hpdca)_2(B\text{-}\beta\text{-}TeW_9O_{33})_2]^{14-}$ in **4a** are connected into a 1-D chain motif by Ln−O−C bonds derived from $Hpdca^-$ ligands (Figure 3). The presence of bridging N and O

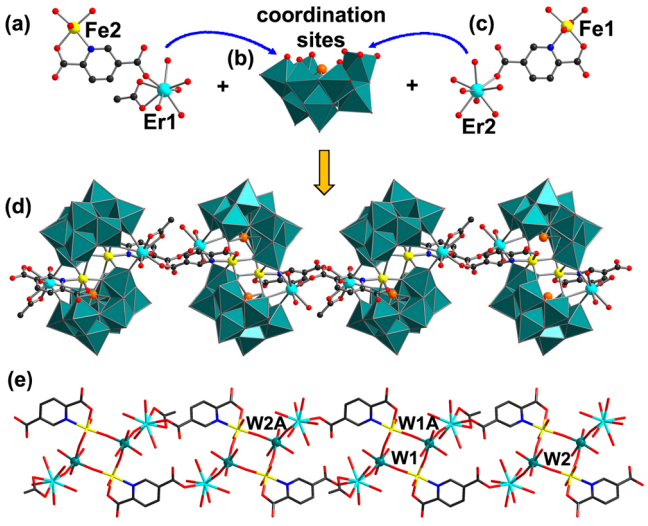

Figure 3. (a, c) The coordination of Ac^- and $Hpdca^-$ ligands with Er^{3+} and Fe^{3+} ions. (b) The $\{TeW_9\}$ fragment with abundant coordination sites. (d) The 1-D chain constructed by **4a** and $Hpdca^-$ bridges. (e) The infinite metal−organic motif constructed by heterometallic clusters and W (W1, W2) atoms. The atom with the suffix A is generated by the symmetry operation, where A: $-x, -y, -z$.

DOI: 10.1021/acs.inorgchem.9b00618
Inorg. Chem. 2019, 58, 9706−9712

atoms by Ac^- and $Hpdca^-$ drive the coordination of metal centers and induce the aggregation of POM intermediates. Note that one crystallographically unique Ac^- ligand is observed in this structure and that each contributes two carboxyl O atoms to coordinate with one $Er1^{3+}$ ion (Figure 3a). In contrast, two crystallographically unique $Hpdca^-$ ligands serve as tridentate ligands. Each of them is combined with the Fe^{3+} ion simultaneously through the O and N atoms to form a stable five-member ring and is further bound to the Er^{3+} ion via the opposite O atom, resulting in two heterometallic clusters $[Er1(Ac)(H_2O)_2\ Fe2(Hpdca)]^{4+}$ ({Er1Fe2}) and $[Er2(H_2O)_4Fe1(Hpdca)]^{5+}$ ({Er2Fe1}) (Figures 3a,c and S6). The $\{TeW_9\}$ fragments with abundant exposed O sites coordinate with these heterometallic clusters to generate the extended architecture with the assistance of Ln−O−C bonds, becoming the first inorganic−organic hybrid TM−Ln heterometallic TTs (Figure 3b,d). Moreover, benefiting from the support of W atoms (W1, W2) from $\{TeW_9\}$ fragments, the connection of $Hpdca^-$ groups facilitates the growth of the heterometallic clusters into an infinite metal−organic motif, along with the formation of different heterometallic cycles (Figure 3e).

Photoluminescence Properties. The unique electronic and structural features of Ln cations make them excellent for photoluminescence (PL).[29] One of the landmarks in this field refers to the discovery of the fluorescent Y_2O_3:Eu^{III} material, which is still in heavy use as phosphors for cathode-ray tubes as well as fluorescent lamps.[30] These findings have stimulated considerable subsequent studies of Ln luminescent materials. Here, the PL measurements for solid-state samples **1** and **2** were performed at ambient temperature.

The emission spectrum of **1** shows three characteristic narrow peaks when excited under 394 nm UV light, corresponding to the $^5D_0 \rightarrow {}^7F_1$ (597 nm), $^5D_0 \rightarrow {}^7F_2$ (614 nm), and $^5D_0 \rightarrow {}^7F_4$ (702 nm) transitions of Eu^{3+} ions, respectively (Figure 4a).[31] Among them, the strongest emission is located at 614 nm and exhibits the red luminescence. Note that the luminescence intensity of $^5D_0 \rightarrow {}^7F_J$ (J = 0, 1, 2, 3, 4) transitions can be used as a probe to judge the site symmetry of the Eu^{3+} ion. Generally, the magnetic-dipole $^5D_0 \rightarrow {}^7F_1$ transition would dominate in the emission spectrum if Eu^{3+} ion occupies inversion-symmetry crystallographic sites, while the preponderant electric-dipole $^5D_0 \rightarrow {}^7F_2$ transition reveals the noninversion center site of the Eu^{3+} ion.[32] Here, the $^5D_0 \rightarrow {}^7F_2$ transition shows the strongest emission at 614 nm, indicating Eu^{3+} ion possesses crystallographic sites without inversion symmetry. This result coincides with the X-ray single-crystal analyses. Several bands are identified in the excitation spectrum at 383, 394, and 416 nm, individually attributable to the $^7F_0 \rightarrow {}^5G_3$, $^7F_0 \rightarrow {}^5L_6$, and $^7F_0 \rightarrow {}^5D_3$ transitions (Figure S7). To get some more information about the PL behavior of **1**, the lifetime decay behavior is obtained by monitoring the excitation at 394 nm and emission at 614 nm, which can be well-fitted to a biexponential function with the equation $I = A_1 \exp(-t/\tau_1) + A_2 \exp(-t/\tau_2)$ (where τ_1 and τ_2 represent the fast and slow components of the luminescence lifetimes, and A_1 and A_2 are the pre-exponential factors), leading to the luminescence lifetimes τ_1 and τ_2 of 10.00 μs (0.52%) and 189.04 μs (99.48%) (Figure 4b). On the basis of $\tau^* = [A_1\tau_1^2 + A_2\tau_2^2]/[A_1\tau_1 + A_2\tau_2]$,[33] the average lifetime τ^* of **1** is calculated to be 188.11 μs.

The solid-state sample of **2** emits the green luminescence under excitation at 376 nm. Its emission spectrum mainly displays two bands at 488 and 546 nm, individually assignable to the $^5D_4 \rightarrow {}^7F_6$ and $^5D_4 \rightarrow {}^7F_6$ transitions of Tb^{3+} ions (Figure 4c).[34] The excitation spectrum of **2** collected by detecting the emission at 546 nm comprises one prominent band at 376 nm, in relation to the $^7F_6 \rightarrow {}^5G_6$ transitions of Tb^{3+} ions (Figure S8).[35] To determine the lifetime behavior of **2**, the luminescence decay curve (Figure 4d) is obtained by monitoring the emission at 546 nm. Evidently, the decay curve also follows the biexponential function, yielding the lifetimes τ_1 and τ_2 of 2.05 μs (59.35%) and 9.72 μs (40.65%), and τ^* is 5.17 μs.

The Commission International d'Eclairage (CIE) 1931 chromaticity coordinates (x, y) of **1** and **2** are determined in regard of their corresponding emission spectra under the 394 and 376 nm excitation, and their values are indexed to (0.540 24, 0.442 44) and (0.428 71, 0.428 30), respectively (Figure S9). Furthermore, some information about the color temperature can be gained from the CIE chromaticity coordinates. The color temperature of a light source can be explained as the surface temperature of an ideal blackbody when emitting a comparable light to that of a light source in visible region. Like intensity, wavelength, and photoperiod, color temperature is also an important characteristic of light, and it has been extensively applied in many realms from photography, videography, and publishing to animal behavior.[36,37] Practically, lamps can be classified into three groups of warm (2900 K), white (4200 K), and cool (6000 K) according to the color temperature, and the color temperature of a light source generally increases when the power in blue part of the spectra is enhanced. Here, the color temperatures of **1** and **2** are calculated to be 1995 and 3278 K, respectively, which belong to the warm hue and compare to those of candlelight (1930 K) and osram lamp (~3000 K) (Figure 5).

The CIE 1931 chromaticity can also be used to describe some other optical properties of a source such as color purity. The dominant wavelength of a light is usually defined as the monochromatic wavelength emitting the closest color as the light. This dominant wavelength can be obtained from the intersection by extending the connective line of the white light point (0.3333, 0.3333) and the light source point to the coordinate curve.[38] Here, the dominant wavelengths of **1** and **2** are 586 and 578 nm (Figure 6), respectively. In addition, the

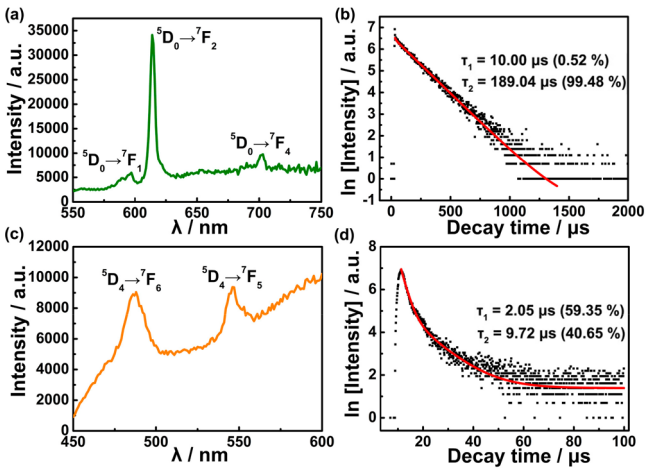

Figure 4. (a) The solid-state emission spectrum of **1** under 394 nm excitation at room temperature. (b) The decay lifetime of **1** by monitoring the emission at 614 nm. (c) The solid-state emission spectrum of **2** under 376 nm excitation at room temperature. (d) The decay lifetime of **2** by monitoring the emission at 546 nm.

DOI: 10.1021/acs.inorgchem.9b00618
Inorg. Chem. 2019, 58, 9706−9712

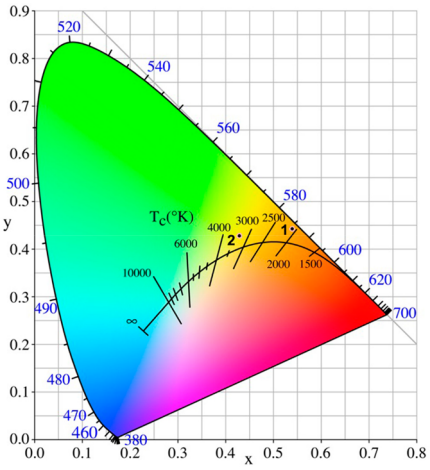

Figure 5. CIE color coordinates of **1** and **2**.

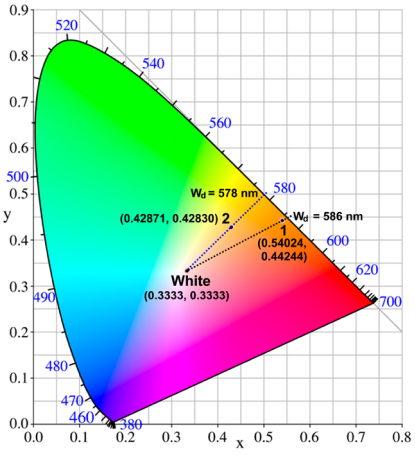

Figure 6. Dominant wavelength (W_d) of **1** and **2** in CIE color coordinates.

color purity (or color saturation), which can express the brightness and shade of color, is determined by the ratio of the distance between light source coordinates (x, y) and white light coordinates (x_i, y_i), and the distance between white light coordinates and dominant wavelength coordinate (x_d, y_d).[39] Thus, the color purity is described by the equation

$$\text{color purity}(\%) = \frac{\sqrt{(x - x_i)^2 + (y - y_i)^2}}{\sqrt{(x_d - x_i)^2 + (y_d - y_i)^2}} \times 100$$

The color purities of **1** and **2** were calculated to be 95.09% and 57.27%. Evidently, **1** exhibits good color purity and is higher than that of **2**, which is in relation to that the color coordinates of **1** emitting orange light is located closer to the coordinate curve. This result also shows that the color purity increases with the increase of the distance from the white light point.

CONCLUSION

In conclusion, benefiting from the synergistic effect of the TeO_3^{2-} heteroanion templates, Ln linkers, and the bridging organic molecules, the first inorganic−organic hybrid 1-D TM−Ln heterometallic TTs $[Ln_2(Ac)_2(H_2O)_4Fe_2(Hpdca)_2(B\text{-}\beta\text{-}TeW_9O_{33})_2][Ln_2(H_2O)_8Fe_2(Hpdca)_2(B\text{-}\beta\text{-}TeW_9O_{33})_2]^{14-}$ [Ln = Eu^{3+} (**1**), Tb^{3+} (**2**), Dy^{3+} (**3**), Er^{3+} (**4**)] were obtained under mild condition. The molecular structural units of **1**−**4** consist of two asymmetric dimeric subunits $[Ln_2(Ac)_2(H_2O)_4Fe_2(Hpdca)_2(B\text{-}\beta\text{-}TeW_9O_{33})_2]^{8-}$ and $[Ln_2(H_2O)_8Fe_2(Hpdca)_2(B\text{-}\beta\text{-}TeW_9O_{33})_2]^{6-}$, in which each subunit is a sandwich-type Fe−Ln heterometallic moiety functionalized by organic components. Magnetic studies indicate a slow relaxation of the magnetization and single-molecule magnet properties of **3**. The PL spectra of **1** and **2** exhibit the typical emission of Ln cation, and the color temperatures of 1995 K for **1** and 3278 K for **2** are in relation to the warm hue. Besides, the dominant wavelengths of 586 and 578 nm and color purities of 95.09% and 57.27% for **1** and **2** are gained. This work provides valuable guidance on the synthesis of novel heterometallic TT derivatives with luminescent and magnetic properties. Currently, our work is focused on other lone-pair-containing system in exploration to construct the TM−Ln heterometallic POM-based derivatives functionalized by different organic ligands with aim at interesting luminescent and magnetic properties.

ASSOCIATED CONTENT

Supporting Information

The Supporting Information is available free of charge on the ACS Publications website at DOI: 10.1021/acs.inorgchem.9b00618.

BVS results of Ln, Fe, and W atoms; partial structural figures; IR spectra and TG analyses of **1**−**4**; luminescence excitation spectra and CIE color coordinates of **1** and **2**; the magnetic properties of **3** (PDF)

Accession Codes

CCDC 1891662−1891665 contain the supplementary crystallographic data for this paper. These data can be obtained free of charge via www.ccdc.cam.ac.uk/data_request/cif, or by emailing data_request@ccdc.cam.ac.uk, or by contacting The Cambridge Crystallographic Data Centre, 12 Union Road, Cambridge CB2 1EZ, UK; fax: +44 1223 336033.

AUTHOR INFORMATION

Corresponding Authors

*E-mail: zhaojunwei@henu.edu.cn. (J.-W.Z.)
*E-mail: songyf@mail.buct.edu.cn; songyufei@hotmail.com. (Y.-F.S.)

ORCID

Jun-Wei Zhao: 0000-0002-7685-1309
Yu-Fei Song: 0000-0003-1309-0626

Notes

The authors declare no competing financial interest.

ACKNOWLEDGMENTS

This research was supported by the National Nature Science Foundation of China (21625101, 21521005, 21771052, 21571048), the National Key Research and Development Program of China (2017YFB0307303), and the Fundamental Research Funds for the Central Universities (XK1802-6, XK1902).

REFERENCES

(1) Pope, M. T. *Heteropoly and Isopoly Oxometalates;* Springer: Berlin, Germany, 1983.
(2) Rhule, J. T.; Hill, C. L.; Judd, D. A.; et al. Polyoxometalates in medicine. *Chem. Rev.* **1998**, *98*, 327−357.

DOI: 10.1021/acs.inorgchem.9b00618
Inorg. Chem. 2019, 58, 9706−9712

(3) Song, Y.-F.; Tsunashima, R. Recent advances on polyoxometalate-based molecular and composite materials. *Chem. Soc. Rev.* **2012**, *41*, 7384−7402.
(4) Ma, P. T.; Hu, F.; Wang, J. P.; Niu, J. Y. Carboxylate covalently modified polyoxometalates: From synthesis, structural diversity to applications. *Coord. Chem. Rev.* **2019**, *378*, 281−309.
(5) Berzelius, J. Beitrag zur näheren Kenntniss des molybdäns. *Ann. Phys.* **1826**, *82*, 369−392.
(6) Miras, H. N.; Richmond, C. J.; Long, D.-L.; Cronin, L. Solution-phase monitoring of the structural evolution of a molybdenum blue nanoring. *J. Am. Chem. Soc.* **2012**, *134*, 3816−3824.
(7) Huang, L.; Wang, S.-S.; Zhao, J.-W.; Cheng, L.; Yang, G.-Y. Synergistic combination of multi-Zr^{IV} cations and lacunary Keggin germanotungstates leading to a gigantic Zr_{24}-cluster-substituted polyoxometalate. *J. Am. Chem. Soc.* **2014**, *136*, 7637−7642.
(8) Liu, J.-C.; Han, Q.; Chen, L.-J.; Zhao, J.-W.; Streb, C.; Song, Y.-F. Aggregation of giant cerium−bismuth tungstate clusters into a 3D porous framework with high proton conductivity. *Angew. Chem., Int. Ed.* **2018**, *57*, 8416−8420.
(9) Wu, Y.-L.; Li, X.-X.; Qi, Y.-J.; Yu, H.; Jin, L.; Zheng, S.-T. $\{Nb_{288}O_{768}(OH)_{48}(CO_3)_{12}\}$: A macromolecular polyoxometalate with close to 300 niobium atoms. *Angew. Chem., Int. Ed.* **2018**, *57*, 8572−8576.
(10) Limanski, E. M.; Drewes, D.; Droste, E.; Böhner, R.; Krebs, B. Syntheses and X-ray characterisation of novel tellurium-substituted lacunary polyoxotungstates containing V^{IV}, Co^{II}, Ni^{II} and Zn^{II} as heteroatoms. *J. Mol. Struct.* **2003**, *656*, 17−25.
(11) Kortz, U.; Al-Kassem, N. K.; Savelieff, M. G.; Al Kadi, N. A.; Sadakane, M. Synthesis and characterization of copper-, zinc-, manganese-, and cobalt-substituted dimeric heteropolyanions, $[(\alpha\text{-}XW_9O_{33})_2M_3(H_2O)_3]^{n-}$ (n = 12, X = As^{III}, Sb^{III}, M = Cu^{2+}, Zn^{2+}; n = 10, X = Se^{IV}, Te^{IV}, M = Cu^{2+}) and $[(\alpha\text{-}AsW_9O_{33})_2WO(H_2O)\text{-}M_2(H_2O)_2]^{10-}$ (M = Zn^{2+}, Mn^{2+}, Co^{2+}). *Inorg. Chem.* **2001**, *40*, 4742−4749.
(12) Kortz, U.; Savelieff, M. G.; Bassil, B. S.; Keita, B.; Nadjo, L. Synthesis and characterization of iron(III)-substituted, dimeric polyoxotungstates, $[Fe_4(H_2O)_{10}(\beta\text{-}XW9O_{33})_2]^{n-}$ (n = 6, X = As^{III}, Sb^{III}; n = 4, X = Se^{IV}, Te^{IV}). *Inorg. Chem.* **2002**, *41*, 783−789.
(13) Cameron, J. M.; Gao, J.; Long, D.-L.; Cronin, L. Self-assembly and structural transformations of high-nuclearity palladium-rich polyoxometalates. *Inorg. Chem. Front.* **2014**, *1*, 178−185.
(14) Zhan, C. H.; Cameron, J. M.; Gao, J.; Purcell, J. W.; Long, D.-L.; Cronin, L. Time-resolved assembly of cluster-in-cluster $\{Ag_{12}\}$-in-$\{W_{76}\}$ polyoxometalates under supramolecular control. *Angew. Chem., Int. Ed.* **2014**, *53*, 10362−10366.
(15) Chen, W.-C.; Li, H.-L.; Wang, X.-L.; Shao, K.-Z.; Su, Z.-M.; Wang, E.-B. Assembly of cerium (III)-stabilized polyoxotungstate nanoclusters with SeO_3^{2-}/TeO_3^{2-} templates: from single polyoxoanions to inorganic hollow spheres in dilute solution. *Chem. - Eur. J.* **2013**, *19*, 11007−11015.
(16) Chen, W.-C.; Qin, C.; Wang, X.-L.; Li, Y.-G.; Zang, H.-Y.; Shao, K.-Z.; Su, Z.-M.; Wang, E.-B. Assembly of a large cerium(III)-containing tungstotellurites(IV) nanocluster: $[Ce_{10}Te_8W_{88}O_{298}(OH)_{12}(H_2O)_{40}]^{18-}$. *Dalton Trans* **2015**, *44*, 11290−11293.
(17) Shang, S. X.; Lin, Z. G.; Yin, A. X.; Yang, S.; Chi, Y. N.; Wang, Y.; Dong, J.; Liu, B.; Zhen, N.; Hill, C. L.; Hu, C. W. Self-assembly of Ln(III)-containing tungstotellurates(VI): correlation of structure and photoluminescence. *Inorg. Chem.* **2018**, *57*, 8831−8840.
(18) Han, Q.; Wen, Y.; Liu, J.-C.; Zhang, W.; Chen, L.-J.; Zhao, J.-W. Rare-earth-incorporated tellurotungstate hybrids functionalized by 2-Picolinic acid ligands: syntheses, structures, and properties. *Inorg. Chem.* **2017**, *56*, 13228−13240.
(19) Han, Q.; Liu, J. C.; Wen, Y.; Chen, L. J.; Zhao, J. W.; Yang, G. Y. Tellurotungstate-based organotin−rare-earth heterometallic hybrids with four organic components. *Inorg. Chem.* **2017**, *56*, 7257−7269.
(20) Liu, J.-L.; Jin, M.-T.; Chen, L.-J.; Zhao, J.-W. First dimethyltin-functionalized rare-earth incorporated tellurotungstates consisting of $\{B\text{-}\alpha\text{-}TeW_7O_{28}\}$ and $\{W_5O_{18}\}$ mixed building units. *Inorg. Chem.* **2018**, *57*, 12509−12520.
(21) Niu, J. Y.; Zhang, S. W.; Chen, H. N.; Zhao, J. W.; Ma, P. T.; Wang, J. P. 1-D, 2-D, and 3-D organic−inorganic hybrids assembled from Keggin-type polyoxometalates and 3d−4f heterometals. *Cryst. Growth Des.* **2011**, *11*, 3769−3777.
(22) Ibrahim, M.; Mereacre, V.; Leblanc, N.; Wernsdorfer, W.; Anson, C. E.; Powell, A. K. Self-assembly of a giant tetrahedral 3d−4f single-molecule magnet within a polyoxometalate system. *Angew. Chem., Int. Ed.* **2015**, *54*, 15574−15578.
(23) Zhao, J.-W.; Cao, J.; Li, Y.-Z.; Zhang, J.; Chen, L.-J. First tungstoantimonate-based transition-metal−lanthanide heterometallic hybrids functionalized by amino acid ligands. *Cryst. Growth Des.* **2014**, *14*, 6217−6229.
(24) Li, T. F.; Wang, Z. L.; Chen, W.; Miras, H. N.; Song, Y.-F. Rational design of a polyoxometalate intercalated layered double hydroxide: highly efficient catalytic epoxidation of allylic alcohols under mild and solvent-free conditions. *Chem. - Eur. J.* **2017**, *23*, 1069−1077.
(25) Zhao, J.-W.; Shi, D. Y.; Chen, L. J.; Li, Y. Z.; Ma, P. T.; Wang, J. P.; Niu, J. Y. Novel polyoxometalate hybrids consisting of copper−lanthanide heterometallic/lanthanide germanotungstate fragments. *Dalton Trans* **2012**, *41*, 10740−10751.
(26) Pan, T.-M.; Chang, W.-T.; Chiu, F.-C. Structural properties and electrical characteristics of high-k Dy_2O_3 gate dielectrics. *Appl. Surf. Sci.* **2011**, *257*, 3964−3968.
(27) Bösing, M.; Nöh, A.; Loose, I.; Krebs, B. Highly efficient catalysts in directed oxygen-transfer processes: synthesis, structures of novel manganese- containing heteropolyanions, and applications in regioselective epoxidation of dienes with hydrogen peroxide. *J. Am. Chem. Soc.* **1998**, *120*, 7252−7259.
(28) Limanski, E. M.; Drewes, D.; Krebs, B. Z. Sandwich-like polyoxotungstates with Indium (III) as a heteroatom-synthesis and characterization of the first examples of a new type of anions. *Z. Anorg. Allg. Chem.* **2004**, *630*, 523−528.
(29) Eliseeva, S. V.; Bünzli, J.-Cl. G. Lanthanide luminescence for functional materials and bio-sciences. *Chem. Soc. Rev.* **2010**, *39*, 189−227.
(30) Shionoya, S.; Yen, W. M. *Phosphor Handbook;* CRC Press Inc.: Boca Raton, FL, 1999.
(31) Liu, J. C.; Yu, J.; Han, Q.; Wen, Y.; Chen, L. J.; Zhao, J. W. First quadruple-glycine bridging mono-lanthanide-substituted borotungstate hybrids. *Dalton Trans* **2016**, *45*, 16471−16484.
(32) Han, B.; Li, P. J.; Zhang, J.; Shi, H. Z. High color purity orange-emitting $KBaBP_2O_8$:Eu^{3+} phosphor: synthesis, characterization and photoluminescence properties. *J. Lumin.* **2014**, *155*, 15−20.
(33) Li, P. L.; Wang, Z. J.; Yang, Z. P.; Guo, Q. L. Tunable blue−green emission phosphor Ca_2PO_4Cl: Ce^{3+}, Tb^{3+}: luminescence and energy transfer. *Opt. Commun.* **2014**, *332*, 83−88.
(34) Xia, J.; Zhao, B.; Wang, H.-S.; Shi, W.; Ma, Y.; Song, H. B.; Cheng, P.; Liao, D. Z.; Yan, S. P. Two- and three-dimensional lanthanide complexes: synthesis, crystal structures, and properties. *Inorg. Chem.* **2007**, *46*, 3450−3458.
(35) Choi, Y. I.; Yoon, Y.; Kang, J.-G.; Sohn, Y. Photoluminescence imaging of Eu(III) and Tb(III)-embedded SiO_2 nanostructures. *J. Lumin.* **2015**, *158*, 27−31.
(36) Wang, Q.; Xu, H.; Zhang, F.; Wang, Z. Influence of color temperature on comfort and preference for LED indoor lighting. *Optik* **2017**, *129*, 21−29.
(37) Kapogiannatou, A.; Paronis, E.; Paschidis, K.; Polissidis, A.; Kostomitsopoulos, N. G. Effect of light color temperature and intensity on the behavior of male C57CL/6J mice. *Appl. Anim. Behav. Sci.* **2016**, *184*, 135−140.
(38) Kumar, J. S.; Pavani, K.; Babu, A. M.; Giri, N. K.; Rai, S. B.; Moorthy, L. R. Fluorescence characteristics of Dy^{3+} ions in calcium fluoroborate glasses. *J. Lumin.* **2010**, *130*, 1916−1923.
(39) Ji, K. M.; Xue, Y. Q.; Cui, Z. X. A new method for colors characterization of colored stainless steel using CIE and Munsell color systems. *Opt. Mater.* **2015**, *47*, 180−184.

DOI: 10.1021/acs.inorgchem.9b00618
Inorg. Chem. 2019, 58, 9706−9712